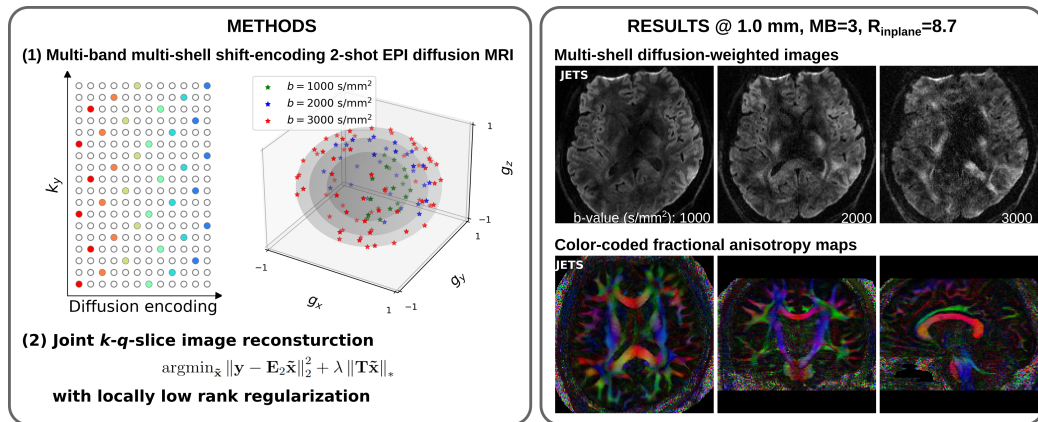


Graphical Abstract

Accelerated Diffusion Magnetic Resonance Imaging at 7 T: Joint Reconstruction for Multi-Shell Multi-Band Shift-Encoded Echo Planar Imaging (JETS-EPI)

Zhengguo Tan, Patrick Alexander Liebig, Robin Martin Heidemann, Frederik Bernd Laun, Florian Knoll



Highlights

Accelerated Diffusion Magnetic Resonance Imaging at 7 T: Joint Reconstruction for Multi-Shell Multi-Band Shift-Encoded Echo Planar Imaging (JETS-EPI)

Zhengguo Tan, Patrick Alexander Liebig, Robin Martin Heidemann, Frederik Bernd Laun, Florian Knoll

- Novel accelerated diffusion acquisition with shifted phase encoding among diffusion directions for complementary k - q -space sampling at 7 T
- Generalized joint k - q -slice diffusion-weighted image reconstruction with overlapping locally low-rank regularization
- 5 min 1.2 mm isotropic resolution with b -value 1000 s/mm^2 and 32 diffusion directions for in vivo whole-brain diffusion tensor imaging
- 23 min 1 mm isotropic resolution with three-shell high b -values (up to 3000 s/mm^2) and 126 diffusion directions for in vivo whole-brain diffusion tensor imaging and fiber tracking

Accelerated Diffusion Magnetic Resonance Imaging at 7 T: Joint Reconstruction for Multi-Shell Multi-Band Shift-Encoded Echo Planar Imaging (JETS-EPI)

Zhengguo Tan^a, Patrick Alexander Liebig^b, Robin Martin Heidemann^b,
Frederik Bernd Laun^c, Florian Knoll^a

^a*Department Artificial Intelligence in Biomedical Engineering (AIBE),
Friedrich-Alexander-Universität Erlangen-Nürnberg (FAU), Erlangen, Germany*

^b*Siemens Healthcare GmbH, Erlangen, Germany*

^c*Institute of Radiology, University Hospital Erlangen, FAU, Erlangen, Germany*

Abstract

The pursuit of high spatial-angular-temporal resolution for in vivo diffusion-weighted magnetic resonance imaging (DW-MRI) at ultra-high field strength (e.g., 7 T) is important in understanding brain microstructure and function. Such pursuit, however, faces several technical challenges. First, increased susceptibility and shorter T_2 relaxation require faster echo train readouts. Second, high angular resolution in q -space requires the use of high and/or multiple b -values, which increases noise in diffusion-weighted images and prolongs scan time. Multi-shot interleaved echo-planar imaging (EPI) and advanced reconstruction strategies, e.g., multiplexed sensitivity-encoding (MUSE) and compressed sensing with structured low-rank matrix completion (MUSSELS), have been proven suitable for high-resolution DW-MRI. These methods, however, do not explore complementary k - q -space sampling and require longer scan time compared to single-shot EPI. To address these challenges, we developed a novel joint reconstruction for multi-shell multi-

band shift-encoding acquisition at 7 T (JETS-EPI). In comparison to MUSE and MUSSELS, it allows for faster acquisition with the use of high inplane acceleration and only two shots per diffusion direction. Moreover, the proposed joint reconstruction exhibits better denoising of DW images and clearer delineation of fiber distributions.

Keywords: Diffusion-weighted magnetic resonance imaging, Echo planar imaging, Ultra high field, Joint reconstruction, Low rank, Simultaneous multi slice

¹ **1. Introduction**

² Diffusion-weighted magnetic resonance imaging (DW-MRI) ([Le Bihan et al., 1986; Merboldt et al., 1985](#)) is a non-invasive modality that is sen-
³ sitive to Brownian motion of water molecules. DW-MRI forms the basis for
⁴ diffusion tensor imaging (DTI) ([Basser et al., 1994; Mori et al., 1999](#)) and
⁵ high angular resolution diffusion imaging (HARDI) ([Tuch et al., 2002](#)), and
⁶ has been widely used in acute brain ischemia diagnosis, in tumor detection
⁷ and staging, and in neuroscience.

⁹ For DW-MRI acquisition, the commonly used pulse sequence is single-
¹⁰ shot echo-planar imaging (SS-EPI) ([Mansfield, 1977](#)). SS-EPI is capable
¹¹ of rapidly acquiring one DW image per radio-frequency excitation at the
¹² order of 100 milliseconds, and is thus motion robust. However, conventional
¹³ SS-EPI, even with three-fold accelerated acquisition ([Bammer et al., 2001](#))
¹⁴ using parallel imaging ([Roemer et al., 1990; Ra and Rim, 1993; Pruessmann et al., 1999; Griswold et al., 2002](#)), still suffers from low spatial resolution
¹⁵ and geometric distortions.

¹⁷ In the quest for high-spatial-angular-resolution and minimal-geometry-
¹⁸ distortion DW-MRI, tremendous efforts have been made. Instead of SS-EPI,
¹⁹ advanced pulse sequences based on multi-shot EPI have been developed, in-
²⁰ cluding but not limited to interleaved EPI ([Butts et al., 1993](#)), PROPELLER
²¹ ([Pipe et al., 2002](#)), readout-segmented EPI ([Porter and Heidemann, 2009; Heidemann et al., 2010](#)), and spiral ([Truong and Guidon, 2014](#)). Multi-shot
²³ EPI acquisition, however, requires not only longer scan time, but also shot-to-
²⁴ shot phase variation correction (due to the use of motion-sensitive diffusion
²⁵ gradients).

26 The standard shot-to-shot phase variation correction acquires navigator
27 echoes at the cost of increased acquisition time. To eliminate this, advanced
28 self-navigated image reconstruction techniques have been developed. Multi-
29 plexed sensitivity encoding (MUSE) based on simultaneous-multi-slice (SMS)
30 (Maudsley, 1980; Breuer et al., 2005) 4-shot interleaved EPI achieved DW-
31 MRI with sub-millimeter inplane resolution and maximal b -value 2000 s/mm²
32 at 3 T (Chen et al., 2013). In MUSE, four shots (i.e., four-fold acceleration
33 per shot) are needed because of two reasons. First, high spatial resolution
34 requires the use of multi-shot acquisition. Second, MUSE employs parallel
35 imaging (e.g. SENSE) to reconstruct shot images for the extraction of shot-
36 to-shot phase variation, and four-fold acceleration per shot is achievable in
37 parallel imaging.

38 Beyond parallel imaging, compressed sensing opens up the possibility of
39 higher acceleration in MRI (Lustig et al., 2007; Block et al., 2007). Multi-shot
40 reconstruction techniques based on structured low-rank matrix completion
41 (MUSSELS) (Mani et al., 2017; Bilgic et al., 2019) achieved 5-shot DW-
42 MRI with 9-fold acceleration per shot. Recently, joint usage of structured
43 low-rank constraints and explicit phase mapping (JULEP) (Dai et al., 2023)
44 incorporated iterative phase update into MUSSELS using 4-shot DW-MRI
45 with 4-fold acceleration per shot. All these techniques target the recon-
46 struction of one DW image from interleaved EPI using at least 4 shots, i.e.,
47 joint- k - q -space acceleration is not explored.

48 Joint- k - q -space acceleration can be achieved via proper regularization
49 along the diffusion encoding direction. Relevant examples are diffusion ac-
50 celeration with Gaussian process estimated reconstruction (DAGER) (Wu

51 et al., 2019) and magnitude-based spatial-angular locally low-rank regular-
52 ization (SPA-LLR) (Hu et al., 2020). DAGER and SPA-LLR address the
53 reconstruction problem of single-shell diffusion data with b -values of 1000
54 and 2000 s/mm^2 , respectively. However, DAGER requires many diffusion
55 directions, whereas SPA-LLR employs the standard interleaved EPI acqui-
56 sition (i.e., all DW acquisition shares the same inplane sampling pattern).
57 Consequently, these techniques still require long acquisition time.

58 In this work, we propose a joint k - q -slice reconstruction framework for
59 multi-band multi-shell shift-encoded EPI at 7 T (dubbed as JETS-EPI).
60 First, our acquisition method differs from most existing techniques as it shifts
61 the k -space in-plane sampling pattern along the phase encoding (k_y) direction
62 per repetition. Such shifting creates complementary k - q -space sampling. Sec-
63 ond, our reconstruction framework generalizes to jointly reconstruct multi-
64 slice multi-shell multi-direction DW images. This is built upon comprehen-
65 sive modeling of the acquisition process and construction of regularization
66 terms (e.g. LLR) as proximal operators. We compared our proposed method
67 with state-of-the-art multi-shot reconstruction techniques, i.e., MUSE and
68 MUSSELS, as well as established DW image denoising algorithms, i.e., lo-
69 cal PCA (Manjón et al., 2013; Veraart et al., 2016). Our proposed method
70 achieves 7 T three-shell high b -value (up to 3000 s/mm^2) and 126 diffusion
71 direction measurements at 1 mm isotropic resolution in less than 23 min.

72 **2. Material and methods**

73 *2.1. Multi-band multi-shell shift-encoded EPI acquisition*

74 Fig. 1 (A) displays an exemplary diffusion weighted image acquisition
75 using two-shot interleaved EPI. Conventionally, such a sampling pattern is
76 repeated for all diffusion directions. In contrast, we propose the k_y -shifted
77 diffusion encoding, as shown in Fig. 1 (B). The interleaved EPI sampling
78 pattern is shifted by one k_y line between diffusion direction, with the cycling
79 period being the acceleration factor per diffusion direction. Fig. 1 (C) dis-
80 plays an exemplary multi-shell sampling pattern. Every diffusion direction is
81 distinct from others, thereby constructing a non-colinear sampling pattern.
82 Such k_y -shifted non-colinear diffusion encoding exploits complementary k -
83 q -space sampling. Its benefits are two-fold. First, the k_y -shifting is linear
84 and retains consistent echo spacing. Second, DW images share anatomical
85 structures but differ in image contrast depending on b -values and diffusion
86 directions, thus complementary q -space sampling is well suited for the explo-
87 ration of structural similarity.

88 *2.2. In vivo acquisition protocols*

89 We implemented multiple in-vivo acquisition protocols at a clinical 7T
90 MR system (MAGNETOM Terra, Siemens Healthineers, Erlangen, Ger-
91 many) equipped with a 32-channel head coil (Nova Medical, Wilmington,
92 MA, USA) and the XR-gradient system (80 mT/m @ 200 T/m/s). To cali-
93 brate coil sensitivity maps, reference scans employed a gradient-echo (GRE)
94 sequence. Fat saturation and mono-polar diffusion-encoding gradients were
95 used. The phase-encoding direction was selected as anterior-to-posterior.

96 This study was approved by the local ethics committee, and informed con-
97 sent was obtained before scanning healthy volunteers. Detailed acquisition
98 parameters are listed below.

99 *2.2.1. Single-shell diffusion acquisition at 1.2 mm isotropic resolution*

100 This protocol employed 220 mm FOV in both read and phase-encoding
101 directions, base resolution 182 mm, 94 slices, bandwidth 1832 Hz/Pixel, echo
102 spacing 0.75 ms, TE 47 ms, TR 4300 ms, 2 shots per diffusion direction, in-
103 plane acceleration 3 as well as partial Fourier 6/8 along the phase-encoding
104 direction, and multi-band factor 2. This results in 8.7×2 fold acceleration
105 per shot. 30 diffusion directions with b -value 1000 s/mm² and 2 diffusion
106 directions with b -value 50 s/mm² were acquired at a total scan time of 5'3".
107 Given the high spatial resolution and the short scan time, this protocol fits
108 well into clinical studies.

109 *2.2.2. Three-shell diffusion acquisition at 1 mm isotropic resolution*

110 This protocol employed the same FOV, shots, inplane acceleration, and
111 partial Fourier as Section 2.2.1. Other parameters were base resolution
112 214 mm, 114 slices, bandwidth 1460 Hz/Pixel, echo spacing 0.81 ms, TE
113 66 ms, TR 5200 ms, and multi-band factor 3. This results in 8.7×3 fold
114 acceleration per shot. As shown in Fig. 1 (C), three shells were sampled
115 by 20, 30, 64 diffusion directions with b -values 1000, 2000, and 3000 s/mm²,
116 respectively. b_0 acquisition was interspersed every ten diffusion directions.
117 This supplies a total of 126 diffusion directions and 22'25" scan time. This
118 protocol demonstrates the capabilities of JETS-EPI in achieving high spatial-
119 angular-temporal resolution and in studying brain microstructure.

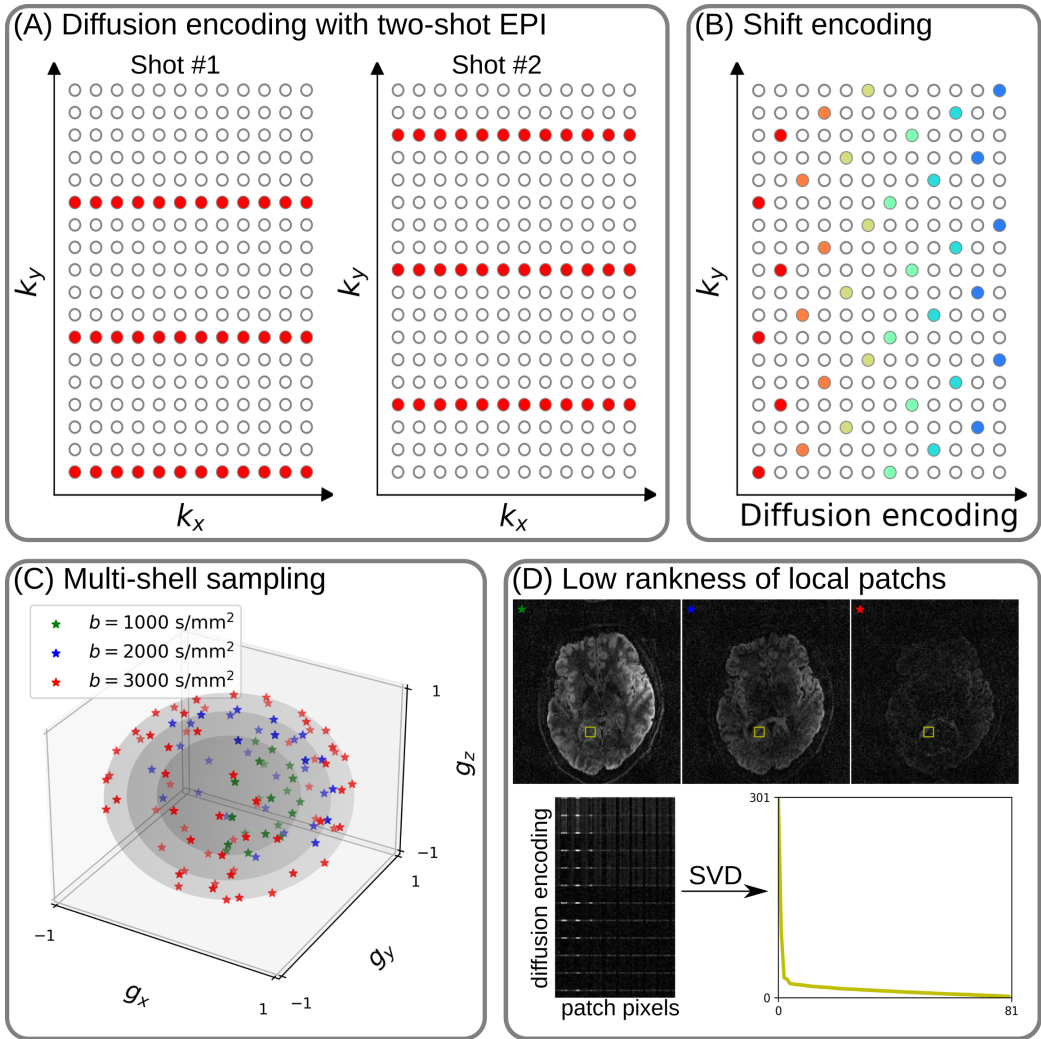


Figure 1: (A) An example DW-MRI acquisition with two-shot interleaved EPI acquisition. (B) The proposed k_y shifted diffusion encoding scheme. This example employs two shots per DW image. Therefore, every two columns have the same color. (C) An example multi-shell sampling scheme. (D) Low rankness of local image patches (as extracted from the yellow blocks) along multi-shell diffusion encoding.

120 *2.3. Forward modeling*

121 Our proposed acquisition method yields multi-dimensional but slice col-
122 lapsed k -space data $\mathbf{y}_{j,q,s}$, where j, q, s denotes the index of the coil sensitivity
123 map, the diffusion encoding, and the shot, respectively. Such acquisition can
124 be modeled in two ways.

First, the acquired k -space data \mathbf{y} is mapped from individual shot images
 $\mathbf{x}_{q,s,z}$ via the forward model,

$$\mathbf{y}_{j,q,s} = \mathbf{P}_{q,s} \boldsymbol{\Sigma} \boldsymbol{\Theta}_z \mathbf{F} \mathbf{S}_j \mathbf{x}_{q,s,z} \quad (1)$$

$$\mathbf{y} := \mathbf{E}_1 \mathbf{x} \quad (2)$$

125 Here, the encoding matrix \mathbf{E}_1 comprises a chain of linear operators. Every
126 shot image \mathbf{x} is point-wise multiplied by a set of coil sensitivity maps (\mathbf{S}) and
127 Fourier transformed (\mathbf{F}). The output is then point-wise multiplied by the
128 multi-slice phase map ($\boldsymbol{\Theta}$) with z the slice index in simultaneously excited
129 slices. This operator shifts individual slice along the phase-encoding direction
130 via varying phase modulation (Breuer et al., 2005). The SMS k -space data
131 is then summed (collapsed, $\boldsymbol{\Sigma}$) along the slice dimension and masked (point-
132 wise multiplied, \mathbf{P}) by the sampling pattern at every diffusion encoding and
133 shot.

134 Second, for diffusion MRI based on multi-shot EPI, shot images per dif-
135 fusion encoding need to be combined as one DW image ($\tilde{\mathbf{x}}$). One method is
136 to perform magnitude average (Chen et al., 2013) or root-sum-squares (RSS)
137 (Mani et al., 2017) of shot images. This method is robust to motion, but
138 sub-optimal with respect to signal-to-noise ratio (SNR) (Guhaniyogi et al.,
139 2016). Alternatively, shot combination is done via shot-to-shot phase vari-
140 ation correction (Liu et al., 2005; Chen et al., 2013). This method can be

₁₄₁ written as point-wise multiplication between the shot-to-shot phase variation
₁₄₂ (Φ) and the DW image ($\tilde{\mathbf{x}}$),

$$\mathbf{x}_{q,s,z} = \Phi_{q,s,z} \tilde{\mathbf{x}}_{q,z} \quad (3)$$

₁₄₃ Note that $\tilde{\mathbf{x}}$ can be obtained by applying the adjoint of Φ to \mathbf{x} . In MUSE,
₁₄₄ Φ is obtained by parallel imaging reconstruction of all shots with subsequent
₁₄₅ phase smoothing of every shot image (e.g. Hanning window). Based on this
₁₄₆ phase correction method, the complete forward model follows

$$\mathbf{y} := \mathbf{E}_2 \tilde{\mathbf{x}} = \mathbf{E}_1 \Phi \tilde{\mathbf{x}} \quad (4)$$

₁₄₇ where the encoding matrix \mathbf{E}_2 comprises the chain of the shot-to-shot phase
₁₄₈ variation Φ and the encoding matrix \mathbf{E}_1 .

₁₄₉ We implemented these two encoding matrices in SigPy ([Ong and Lustig, 2019](#)), utilizing the concept of object-oriented linear operator abstraction.

₁₅₁ 2.4. Joint k - q -slice reconstruction

₁₅₂ Based on the generalized forward models in Eqs. (2) and (4), our proposed
₁₅₃ joint k - q -slice reconstruction can be formulated as a three-step approach.

₁₅₄ I. Joint reconstruction of all shot images by solving the following inverse
₁₅₅ problem with the LLR regularization:

$$\operatorname{argmin}_{\mathbf{x}} \|\mathbf{y} - \mathbf{E}_1 \mathbf{x}\|_2^2 + \lambda \|\mathbf{T} \mathbf{x}\|_* \quad (5)$$

₁₅₆ Note that this step suffices in the case of single-shot EPI acquisition.
₁₅₇ II. For multi-shot EPI acquisition, shot-to-shot phase variation is extracted
₁₅₈ from \mathbf{x} . As phase images are spatially smooth ([Chen et al., 2013; Dai](#)



159 et al., 2023), only the central 1/4-FOV k -space region of \mathbf{y} is used to
 160 solve for \mathbf{x} . To obtain shot phases, the reconstructed \mathbf{x} is interpolated to
 161 the full \mathbb{V} . The corresponding phase is then filtered by the Hanning
 162 window.

163 III. Joint reconstruction of all DW images using the shot-combined forward
 164 model \mathbf{E}_2 with shot-to-shot phase variation from Step II:

$$\operatorname{argmin}_{\tilde{\mathbf{x}}} \|\mathbf{y} - \mathbf{E}_2 \tilde{\mathbf{x}}\|_2^2 + \lambda \|\mathbf{T} \tilde{\mathbf{x}}\|_* \quad (6)$$

165 *2.5. Locally low rank (LLR) regularization*

166 As shown in Fig. 1 (D), low rankness exists in local patches from multi-
 167 shell DW images. Intuitively, low rankness comes from the contrast variation
 168 feature of DW images. This motivates the application of LLR regularization
 169 (Trzasko and Manduca, 2011; Zhang et al., 2015) for solving the inverse
 170 problems in Eqs. (5) and (6). Here, λ is the regularization strength ($\lambda \geq 0$).
 171 \mathbf{T} represents a linear operator that firstly slides a local patch window through
 172 all DW images and then flattens every set of local patches to two-dimensional
 173 (2D) matrices. The nuclear norm regularization is enforced via singular value
 174 thresholding of all flattened 2D matrices (Cai et al., 2010). We implemented
 175 this regularization term as an proximal operator (Beck, 2017).

176 Noteworthy, it has been reported that LLR is prone to checkerboard
 177 artifacts when λ is too large (Hu et al., 2020). We overcome this problem
 178 utilizing overlapping blocks and provide an efficient implementation. If the
 179 blocks overlap, $\mathbf{T}^H \mathbf{T}$ input \neq input, where \mathbf{T}^H denotes the adjoint operator
 180 of \mathbf{T} . Our efficient implementation is to scale \mathbf{T}^H as $(\mathbb{F} \text{ divisor}) \mathbf{T}^H$, where
 181 the divisor matrix is obtained by $\mathbf{T}^H \mathbf{T} \mathbf{1}$. $\mathbf{1}$ denotes the matrix of ones with
 182 the same shape as input.

183 2.6. Reconstruction

184 The acquired raw data was read in by twixtools (<https://github.com/pehses/twixtools>). Ramp-sampling regridding and FOV/2-ghost correction were also performed in twixtools. Subsequently, coil sensitivity maps were computed from reference scans using ESPIRiT (Uecker et al., 2014) in SigPy (Ong and Lustig, 2019).

189 With this pre-processing as well as the implemented forward models and
 190 the proximal operator, both inverse problems in Eqs. (5) and (6) were solved
 191 by the alternating direction method of multipliers (ADMM) (Boyd et al.,
 192 2010).

193 ADMM solves the minimization problems in an alternating update scheme,

$$\begin{cases} \mathbf{x}^{(k+1)} := \underset{\mathbf{x}}{\operatorname{argmin}} \| \mathbf{y} - \mathbf{E}(\mathbf{x}) \|_2^2 + \rho/2 \| \mathbf{T}\mathbf{x} - \mathbf{z}^{(k)} + \mathbf{u}^{(k)} \|_2^2 \\ \mathbf{z}^{(k+1)} := \mathcal{T}_{\lambda/\rho}(\mathbf{T}\mathbf{x}^{(k+1)} + \mathbf{u}^{(k)}) \\ \mathbf{u}^{(k+1)} := \mathbf{u}^{(k)} + \mathbf{T}\mathbf{x}^{(k+1)} - \mathbf{z}^{(k+1)} \end{cases} \quad (7)$$

194 where k denotes the ADMM iteration. Note that \mathbf{x} can be solved using linear
 195 least square algorithms, e.g. conjugate gradient (Hestenes and Stiefel, 1952),
 196 while \mathbf{z} is updated via singular value thresholding. The coupling parameter ρ
 197 is effective in both the update of \mathbf{x} and \mathbf{z} . It acts as Tikhonov regularization
 198 strength when updating \mathbf{x} , but also inversely scales the thresholding strength
 199 when updating \mathbf{z} , ss shown in Supporting Information Figures S1 and S2.

200 In this work, 15 ADMM iterations with $\rho = 0.05$ and $\lambda = 0.04$, and a
 201 block size of 6 for LLR (refer to Supporting Information Figure S3) were
 202 used. All reconstructions were done on a single A100 SXM4/Nvlink GPU
 203 with 40 GB memory (NVIDIA, Santa Clara, CA, USA).

204 We compared our proposed joint reconstruction with established multi-
205 shot reconstruction techniques, i.e. MUSE (Chen et al., 2013) and MUSSELS
206 (Mani et al., 2017). We implemented both techniques in Python and vali-
207 dated them with open-source codes and data (Dai et al., 2023; Bilgic et al.,
208 2019). For implementation details, please refer to "Reproducing MUSE
209 and MUSSELS in Python" in the Supporting Information. Further, we de-
210 noised MUSE diffusion-weighted images with local PCA (Manjón et al., 2013;
211 Veraart et al., 2016).

212 With reconstructed DW images, fractional anisotropy (FA) maps (Basser
213 et al., 1994) were fitted using our implementation in Python, whereas fiber
214 orientation distribution functions (fODF) (Tournier et al., 2007) were com-
215 puted in DIPY (Garyfallidis et al., 2014). 

216 **3. Results**

217 *3.1. Single-shell diffusion acquisition at 1.2 mm isotropic resolution*

218 Fig. 2 displays a DW image for one diffusion direction and zoomed-in
219 colored FA maps from MUSE, MUSE with denoising, MUSSELS, and JETS
220 reconstruction. Both MUSE and MUSSELS exhibit residual noise artifacts
221 for the single-shell acquisition with the b -value of 1000 s/mm². The local PCA
222 denoiser removes noise, but the denoised DW image loses fine structures,
223 e.g. the cuneus (highlighted by the low arrow in the figure). This over-
224 smoothing effect can also be observed in the colored FA map, where the thin
225 fibers near to gray matter are missing.

226 *3.2. Three-shell diffusion acquisition at 1.0 mm isotropic resolution*

227 Results for a 1.0 mm isotropic resolution three-shell 126-direction diffusion
228 acquisition are shown in Fig. 3. At this resolution, severe reduction of signal-
229 to-noise ratio (SNR) can be observed for higher b -values. With such low SNR
230 levels, brain structures are completely buried below the noise level in MUSE
231 and MUSSELS. The local PCA denoiser removes noise efficiently from the
232 reconstructed MUSE images, but images from higher b -values suffer from
233 severe blurring that leads to a loss of fine image details. Only the proposed
234 JETS method with the combination of the k_y -shift encoding scheme and LLR
235 regularized reconstruction allows to resolve brain features for higher b -values.

236 Fig. 4 shows fitted FA maps in three orthogonal orientations based on the
237 above four DW image reconstruction methods. Corresponding color-coded
238 FA maps are provided in Supporting Information Figure S6. All FA maps
239 are displayed with the same windowing, i.e., minimal and maximal values set

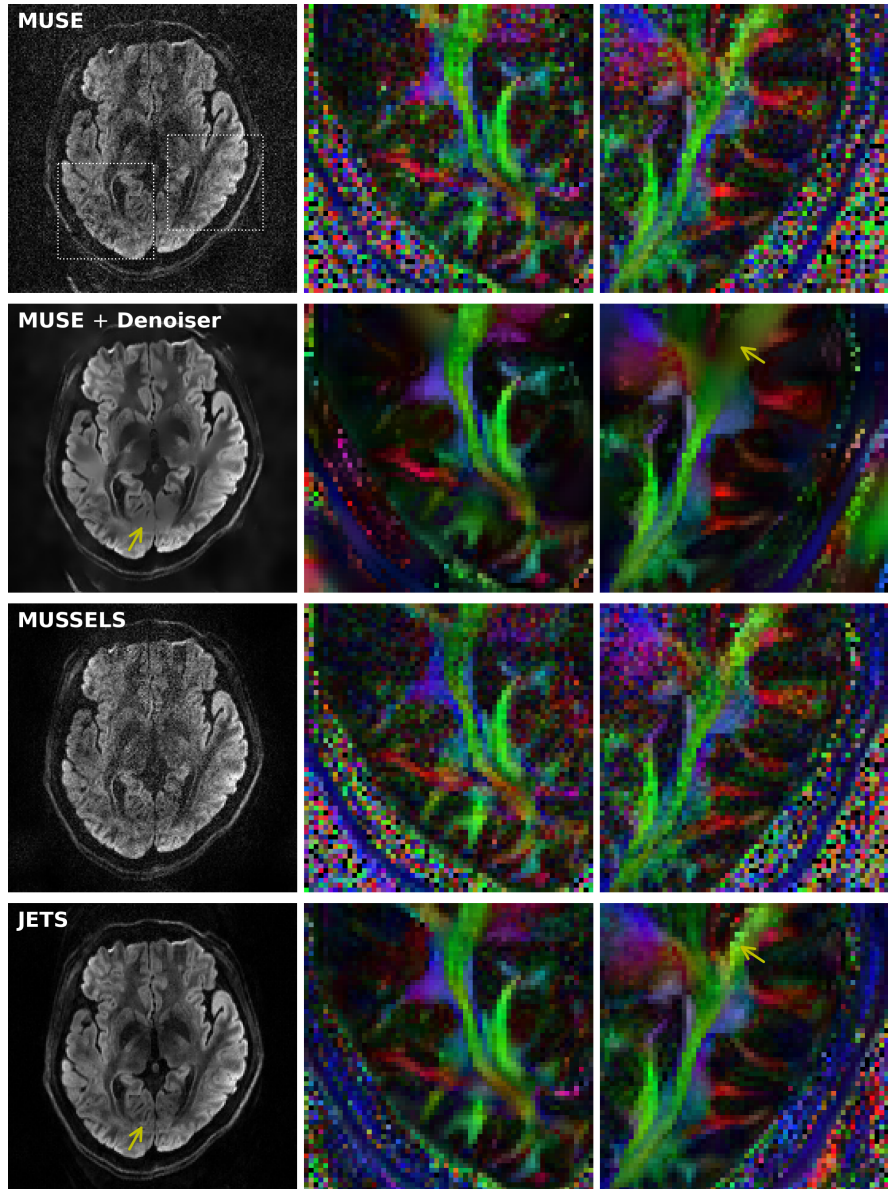


Figure 2: Comparison of reconstructions of a single-shell diffusion acquisition at 1.2 mm isotropic resolution: (1st row) MUSE, (2nd row) MUSE with local PCA denoising, (3rd row) MUSSELS, and (4th row) our proposed JETS approach. The DW image of the 42nd slice and 24th diffusion direction and its zoomed-in colored fractional anisotropy (FA) maps (dashed rectangles) are displayed. The denoiser over-smoothes the images, resulting in missing thin veins and fibers (indicated by yellow arrows).

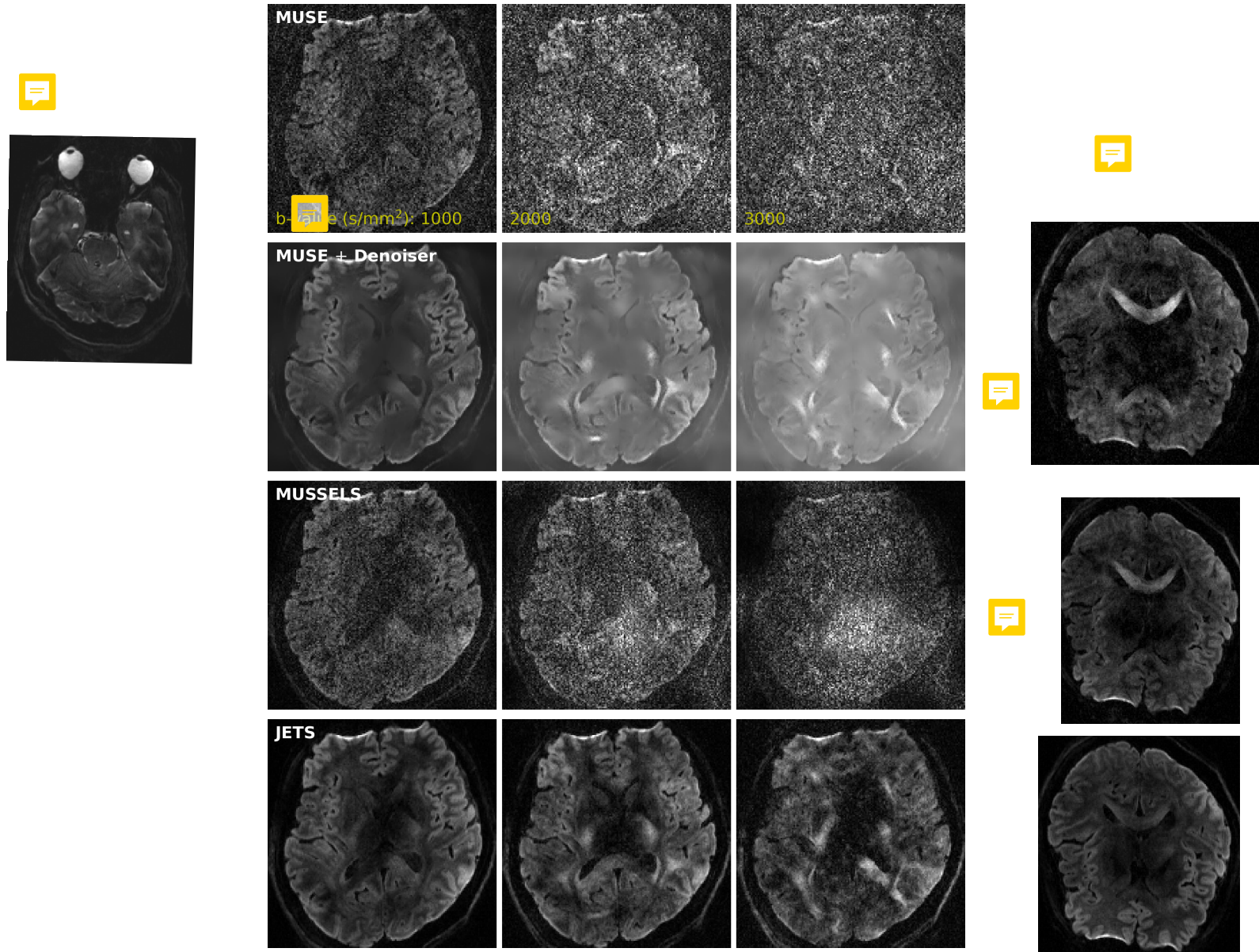


Figure 3: Comparison of reconstructed DW images on three-shell diffusion acquisition at 1 mm isotropic resolution. DW images of the 60th slice for one diffusion direction at different b -values are displayed: (left) 1000, (center) 2000, and (right) 3000 s/mm^2 .

240 as 0 and 1, respectively. The FA maps from MUSE with local PCA desnoising
241 exhibit much lower values than other methods. This may be caused by the
242 excessive noise in DW images from MUSE and by noise estimate in the local
243 PCA denoising algorithm (Veraart et al., 2016). Among all methods, FA
244 maps from JETS show better quality and delineate fine details within the
245 putamen (see white arrows).

246 Fig. 5 shows fODF peaks (Tournier et al., 2007; Garyfallidis et al., 2014)
247 for the ROIs indicated by the dashed rectangles in the axial and the sagittal
248 directions in Fig. 4, respectively. These maps provide further insights into
249 the properties of the evaluated methods.

250 First, noisy DW images from both MUSE and MUSSELS reconstructions
251 result in chaotic fiber orientation in the axial slice in Fig. 4. The local PCA
252 denoiser reduces noise in the DW images, but its corresponding fODF peaks
253 again show over-smoothing effects. In contrast, JETS correctly delineates
254 crossing fibers in the white matter (indicated by the white arrow). Second,
255 fODF peaks in mid-sagittal cross-sections of the corpus callosum exhibit
256 varying fiber densities, which is especially clear in JETS. This shows good
257 agreement with the established topographical distribution (Hofer and Frahm,
258 2006).

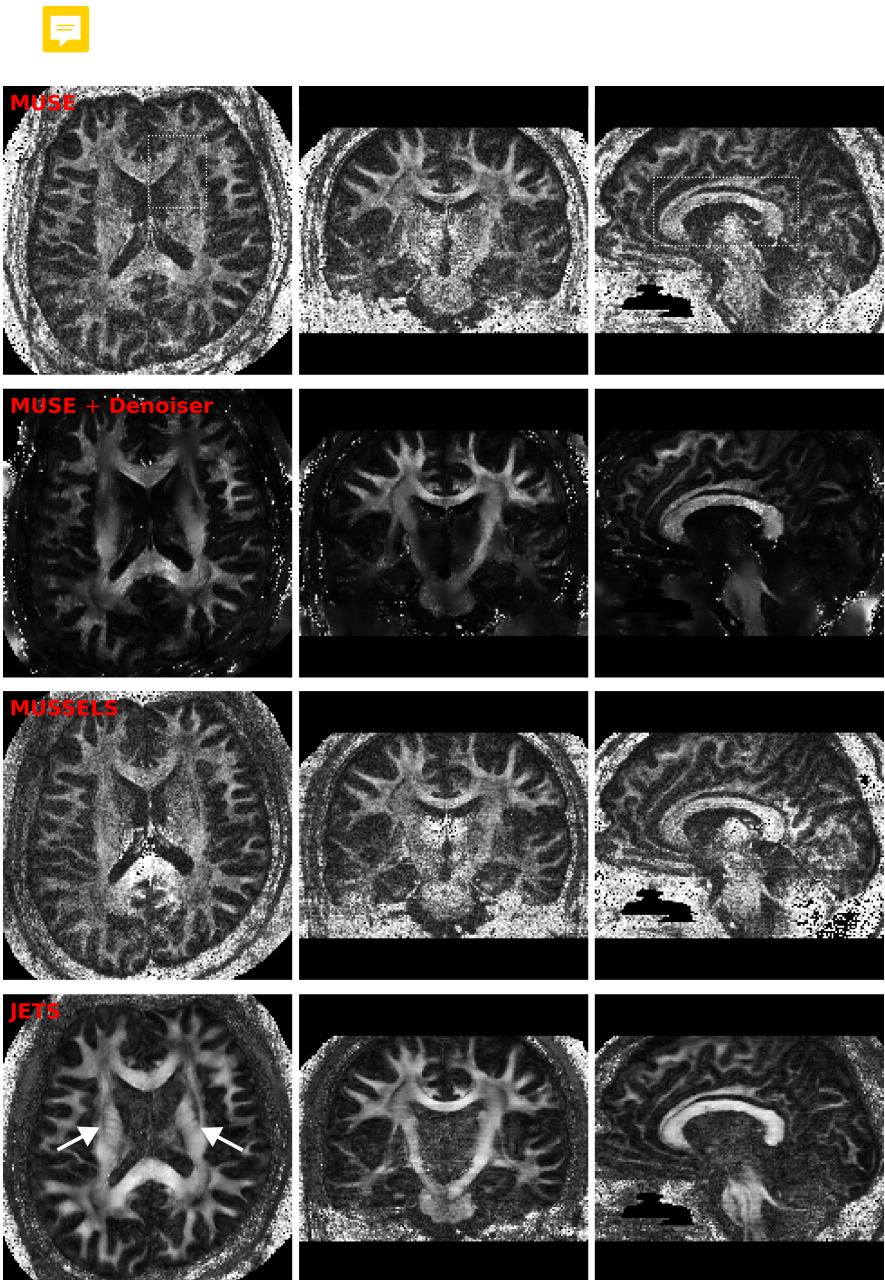


Figure 4: Comparison of reconstructed FA maps based on the 1 mm isotropic resolution three-shell diffusion acquisition. One slice from every orientation (axial, coronal, and sagittal view from left to right) was selected for display.

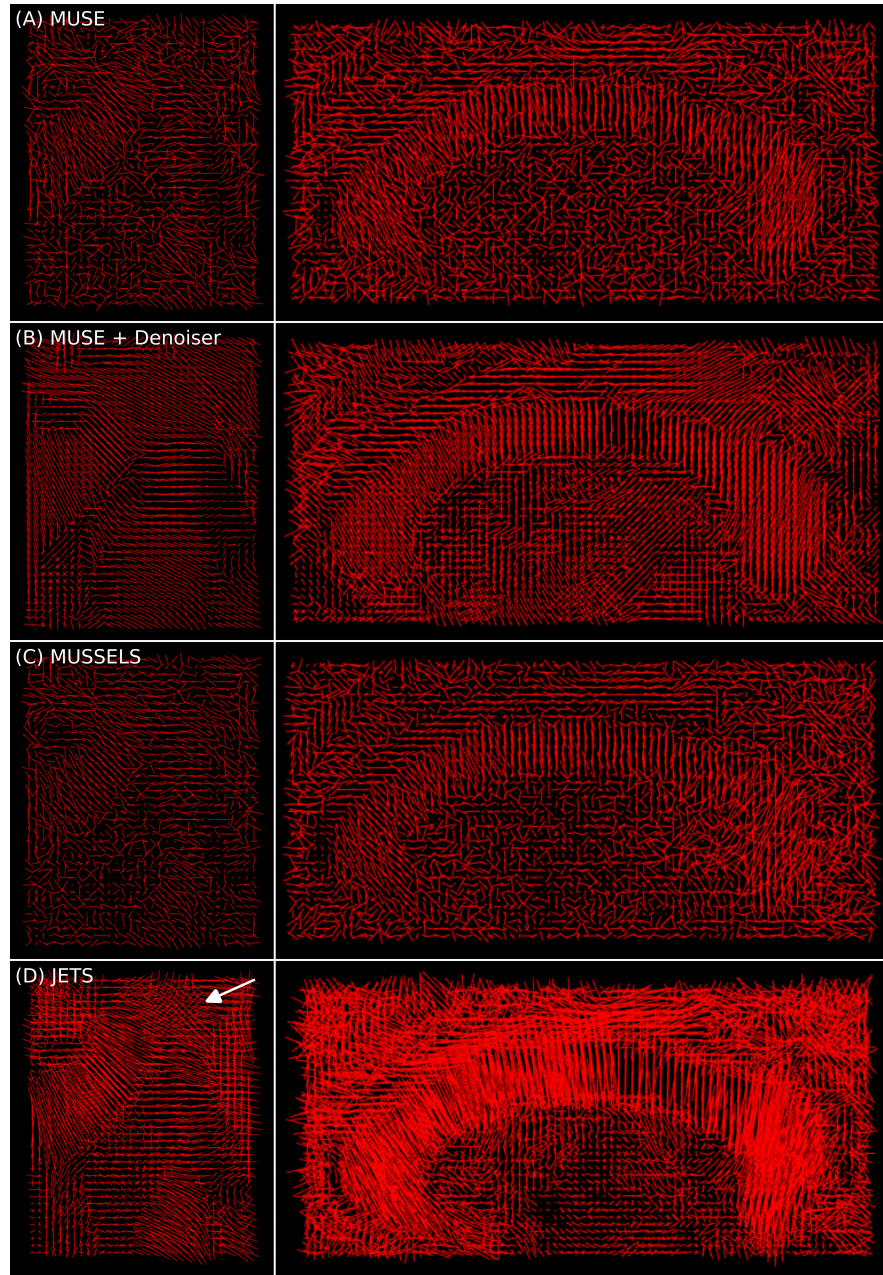


Figure 5: Comparison of fODF peaks within the dashed rectangles of the axial and the sagittal slices in Fig. 4, respectively.

259 **4. Discussion**

260 This work reports a novel DW-MRI technique, dubbed as JETS-EPI,
261 comprising two ingredients, multi-band k_y -shift-encoded interleaved EPI for
262 complementary k - q -space sampling, and a generalized joint reconstruction
263 with overlapping locally low-rank regularization to explore low rankness along
264 the diffusion encoding dimension. JETS-EPI utilizes only two shots per
265 diffusion direction, thereby allowing for short scan time as well as high spatial
266 resolution with reduced geometric distortion. Our reconstruction achieves
267 8.7×3 ($R_{\text{inplane}} \times \text{SMS}$) fold accelerated brain DW-MRI at 7 T with 1 mm
268 isotropic resolution and 126 diffusion-direction (three shells with b -values of
269 1000, 2000, and 3000 s/mm²) in less than 23 min.

270 The reconstruction results from MUSE and MUSSELS suffer from noise
271 effects in this study, and the reasons are two-fold. First, the high in-plane
272 acceleration factor per shot hinders shot-to-shot phase variation estimation
273 in MUSE, whereas we proposed to jointly reconstruct all shot images from
274 the central k -space data. Further, joint reconstruction benefits from the
275 complementary k - q -space sampling, as compared to the shot-by-shot parallel
276 imaging reconstruction. Second, structured low-rank matrix completion as
277 MUSSELS usually works with at least four shots per diffusion direction,
278 whereas this study uses only two shots. The use of two shots is beneficial
279 for shorter scan time than four shots, but hinders the structured low rank
280 property in MUSSELS.

281 One limitation of JETS-EPI is the long reconstruction time due to the
282 simultaneous reconstruction of all DW images and the use of overlapping
283 locally low-rank regularization. The reconstruction of the protocols in Sec-

tion 2.2.1 and Section 2.2.2 on GPU A100 takes about 0.5 h and 3 h per collapsed slice, respectively. To reduce the computation time, coil compression algorithms (Huang et al., 2008) can be employed to reduce the number of coils for image reconstruction. Moreover, one may deploy multi-GPU distributed computing or modern optimization algorithms (e.g. stochastic gradient descent) (Ong et al., 2020) to speed up the reconstruction.

While this work reconstructs all DW images and then performs model fitting, an alternative approach is to directly estimate b_0 and diffusion tensors from measured k - q -space data using model-based reconstruction (Knoll et al., 2015; Dong et al., 2018; Shafieizargar et al., 2023). Compared to DW image reconstruction, model-based reconstruction solves for fewer number of unknowns, but requires strict diffusion tensor modeling and the use of nonlinear least square solvers.

5. Conclusions

We demonstrated the JETS-EPI technique, which integrates a k_y -shifted encoding interleaved EPI sequence and a joint reconstruction with overlapping locally low-rank regularization for high spatial-angular-temporal resolution DW-MRI at 7T. This technique requires no phase navigation, and allows for high quality DW image reconstruction with accelerated acquisition.

Funding

This work was supported by [xxx](#).

306 **Data and code available statement**

307 In the spirit of reproducible and open science, we will publish our source
308 code (<https://github.com/ZhengguoTan/sigpy>) as well as the raw k -space
309 data during the review process.

310 **Acknowledgments**

311 The authors gratefully acknowledge the scientific support and HPC re-
312 sources provided by the Erlangen National High Performance Computing
313 Center (NHR@FAU) of Friedrich-Alexander-Universität Erlangen-Nürnberg
314 (FAU) under the NHR project <ID of your NHR@FAU project>. NHR
315 funding is provided by federal and Bavarian state authorities. NHR@FAU
316 hardware is partially funded by the German Research Foundation (DFG) –
317 440719683.

318 **References**

- 319 Bammer, R., Keeling, S.L., Augustin, M., Pruessmann, K.P., Wolf, R., Stoll-
320 berger, R., Hartung, H.P., Fazekas, F., 2001. Improved diffusion-weighted
321 single-shot echo-planar imaging (EPI) in stroke using sensitivity encoding
322 (SENSE). Magn. Reson. Med. 46, 548–554. doi:[10.1002/mrm.1226](https://doi.org/10.1002/mrm.1226).
- 323 Basser, P.J., Mattiello, J., Le Bihan, D., 1994. MR diffusion tensor
324 spectroscopy and imaging. Biophys. J. 66, 259–267. doi:[10.1016/S0006-3495\(94\)80775-1](https://doi.org/10.1016/S0006-3495(94)80775-1).

- 326 Beck, A., 2017. First-order methods in optimization. Society for In-
327 dustrial and Applied Mathematics, Philadelphia, PA. doi:[10.1137/1.9781611974997](https://doi.org/10.1137/1.9781611974997).
- 329 Bilgic, B., Chatnuntawech, I., Manhard, M.K., Tian, Q., Liao, C., Iyer, S.S.,
330 Cauley, S.F., Huang, S.Y., Polimeni, J.R., Wald, L.L., Setsompop, K.,
331 2019. Highly accelerated multishot echo planar imaging through synergistic
332 machine learning and joint reconstruction. Magn. Reson. Med. 82, 1343–
333 1358. doi:[10.1002/mrm.27813](https://doi.org/10.1002/mrm.27813).
- 334 Block, K.T., Uecker, M., Frahm, J., 2007. Undersampled radial MRI with
335 multiple coils. Iterative image reconstruction using a total variation con-
336 straint. Magn. Reson. Med. 57, 1186–1098. doi:[10.1002/mrm.21236](https://doi.org/10.1002/mrm.21236).
- 337 Boyd, S., Parikh, N., Chu, E., Peleato, B., Eckstein, J., 2010. Distributed
338 optimization and statistical learning via the alternating direction method
339 of multipliers. Foundations and Trends in Machine Learning 3, 1–122.
340 doi:[10.1561/2200000016](https://doi.org/10.1561/2200000016).
- 341 Breuer, F.A., Blaimer, M., Heidemann, R.M., Mueller, M.F., Griswold, M.A.,
342 Jakob, P.M., 2005. Controlled Aliasing in Parallel Imaging Results in
343 Higher Acceleration (CAIPIRINHA) for Multi-Slice Imaging. Magn. Re-
344 son. Med. 53, 684–691. doi:[10.1002/mrm.20401](https://doi.org/10.1002/mrm.20401).
- 345 Butts, K., Riederer, S.J., Ehman, R.L., Thompson, R.M., Jack, C.R., 1993.
346 Interleaved echo planar imaging on a standard MRI system. Magn. Reson.
347 Med. 31, 67–72. doi:[10.1002/mrm.1910310111](https://doi.org/10.1002/mrm.1910310111).

- 348 Cai, J.F., Candès, E.J., Shen, Z., 2010. A singular value thresholding
349 algorithm for matrix completion. SIAM. J. Optim. 20, 1956–1982.
350 doi:[10.1137/080738970](https://doi.org/10.1137/080738970).
- 351 Chen, N.K., Guidon, A., Chang, H.C., Song, A.W., 2013. A robust multi-
352 shot scan strategy for high-resolution diffusion weighted MRI enabled by
353 multiplexed sensitivity-encoding (MUSE). NeuroImage 72, 41–47. doi:[10.1016/j.neuroimage.2013.01.038](https://doi.org/10.1016/j.neuroimage.2013.01.038).
- 355 Dai, E., Mani, M., McNab, J.A., 2023. Multi-band multi-shot diffu-
356 sion MRI reconstruction with joint usage of structured low-rank con-
357 straints and explicit phase mapping. Magn. Reson. Med. 89, 95–111.
358 doi:[10.1002/mrm.29422](https://doi.org/10.1002/mrm.29422).
- 359 Dong, Z., Dai, E., Wang, F., Zhang, Z., Ma, X., Yuan, C., Guo, H., 2018.
360 Model-based reconstruction for simultaneous multislice and parallel imag-
361 ing accelerated multishot diffusion tensor imaging. Med. Phys. 45, 3196–
362 3204. doi:[10.1002/mp.12974](https://doi.org/10.1002/mp.12974).
- 363 Garyfallidis, E., Brett, M., Amirbekian, B., Rokem, A., van der Walt, S.,
364 Descoteaux, M., Nimmo-Smith, I., Contributors, D., 2014. DIPY, a library
365 for the analysis of diffusion MRI data. Front. Neuroinform. 8, 1–17. doi:[10.3389/fninf.2014.00008](https://doi.org/10.3389/fninf.2014.00008).
- 367 Griswold, M.A., Jakob, P.M., Heidemann, R.M., Nittka, M., Jellus, V.,
368 Wang, J., Kiefer, B., Haase, A., 2002. Generalized autocalibrating par-
369 tially parallel acquisitions (GRAPPA). Magn. Reson. Med. 47, 1202–1210.
370 doi:[10.1002/mrm.10171](https://doi.org/10.1002/mrm.10171).

- 371 Guhaniyogi, S., Chu, M.L., Chang, H.C., Song, A.W., Chen, N.K., 2016. Motion
372 immune diffusion imaging using augmented MUSE for high-resolution
373 multi-shot EPI. *Magn. Reson. Med.* 75, 639–652. doi:[10.1002/mrm.25624](https://doi.org/10.1002/mrm.25624).
- 374 Heidemann, R.M., Porter, D.A., Anwander, A., Feiwei, T., Heberlein, K.,
375 Knösche, T.R., Turner, R., 2010. Diffusion imaging in humans at 7 T
376 using readout-segmented EPI and GRAPPA. *Magn. Reson. Med.* 64, 9–
377 14. doi:[10.1002/mrm.22480](https://doi.org/10.1002/mrm.22480).
- 378 Hestenes, M.R., Stiefel, E., 1952. Methods of conjugate gradients for solving
379 linear systems. *J. Res. Natl. Bur. Stand.* 49, 409–436. doi:[10.6028/jres.049.044](https://doi.org/10.6028/jres.049.044).
- 380
- 381 Hofer, S., Frahm, J., 2006. Topography of the human corpus callosum revisited – Comprehensive fiber tractography using diffusion tensor magnetic
382 resonance imaging. *NeuroImage* 32, 989–994. doi:[10.1016/j.neuroimage.2006.05.044](https://doi.org/10.1016/j.neuroimage.2006.05.044).
- 383
- 384
- 385 Hu, Y., Wang, X., Tian, Q., Yang, G., Daniel, B., McNab, J., Hargreaves, B.,
386 2020. Multi-shot diffusion-weighted MRI reconstruction with magnitude-
387 based spatial-angular locally low-rank regularization (SPA-LLR). *Magn.*
388 *Reson. Med.* 83, 1596–1607. doi:[10.1002/mrm.28025](https://doi.org/10.1002/mrm.28025).
- 389
- 390 Huang, F., Vijayakumar, S., Li, Y., Hertel, S., Duensing, G.R., 2008. A soft-
391 ware channel compression technique for faster reconstruction with many
392 channels. *Magn. Reson. Imaging* 26, 133–141.
- 393
- Knoll, F., Raya, J.G., Halloran, R.O., Baete, S., Sigmund, E., Bammer, R.,
Block, T., Otazo, R., Sodickson, D.K., 2015. A model-based reconstruction

- 394 for undersampled radial spin-echo DTI with variational penalties on the
395 diffusion tensor. NMR Biomed 28, 353–366.
- 396 Le Bihan, D., Breton, E., Lallemand, D., Grenier, P., Cabanis, E., Laval-
397 Jeantet, M., 1986. MR imaging of intravoxel incoherent motions: appli-
398 cation to diffusion and perfusion in neurologic disorders. Radiology 161,
399 401–407. doi:[10.1148/radiology.161.2.3763909](https://doi.org/10.1148/radiology.161.2.3763909).
- 400 Liu, C., Moseley, M.E., Bammer, R., 2005. Simultaneous phase cor-
401 rection and SENSE reconstruction for navigated multi-shot DWI with
402 non-Cartesian k -space sampling. Magn. Reson. Med. 54, 1412–1422.
403 doi:[10.1002/mrm.20706](https://doi.org/10.1002/mrm.20706).
- 404 Lustig, M., Donoho, D., Pauly, J.M., 2007. Sparse MRI: The application of
405 compressed sensing for rapid MR imaging. Magn. Reson. Med. 58, 1182–
406 1195. doi:[10.1002/mrm.21391](https://doi.org/10.1002/mrm.21391).
- 407 Mani, M., Jacob, M., Kelley, D., Magnotta, V., 2017. Multi-shot sensitivity-
408 encoded diffusion data recovery using structured low-rank matrix comple-
409 tion (MUSSELS). Magn. Reson. Med. 78, 494–507. doi:[10.1002/mrm.26382](https://doi.org/10.1002/mrm.26382).
- 410
- 411 Manjón, J.V., Coupé, P., Concha, L., Buades, A., Collins, D.L., Robles, M.,
412 2013. Diffusion weighted image denoising using overcomplete local PCA.
413 PLoS One 8, e73021. doi:[10.1371/journal.pone.0073021](https://doi.org/10.1371/journal.pone.0073021).
- 414 Mansfield, P., 1977. Multi-planar image formation using NMR spin echoes.
415 J Phys C 10, 55–58. doi:[10.1088/0022-3719/10/3/004](https://doi.org/10.1088/0022-3719/10/3/004).

- ⁴¹⁶ Maudsley, A.A., 1980. Multiple-line-scanning spin density imaging. *J. Magn.*
⁴¹⁷ *Reson.* 41, 112–126. doi:[10.1016/0022-2364\(80\)90207-3](https://doi.org/10.1016/0022-2364(80)90207-3).
- ⁴¹⁸ Merboldt, K.D., Hanicke, W., Frahm, J., 1985. Self-diffusion NMR imaging using stimulated echoes. *J. Magn. Reson.* 64, 479–486. doi:[10.1016/0022-2364\(85\)90111-8](https://doi.org/10.1016/0022-2364(85)90111-8).
- ⁴²¹ Mori, S., Crain, B.J., Chacko, V.P., Van Zijl, P.C.M., 1999. Three-dimensional tracking of axonal projections in the brain by magnetic resonance imaging. *Ann. Neurol.* 45, 265–269. doi:[10.1002/1531-8249\(199902\)45:2<265::AID-ANA21>3.0.CO;2-3](https://doi.org/10.1002/1531-8249(199902)45:2<265::AID-ANA21>3.0.CO;2-3).
- ⁴²⁵ Ong, F., Lustig, M., 2019. SigPy: A Python package for high performance iterative reconstruction, in: Proceedings of the 27th Annual Meeting of ISMRM, Montréal, CAN, p. 4819.
- ⁴²⁸ Ong, F., Zhu, X., Cheng, J.Y., Johnson, K.M., Larson, P.E.Z., Vasanawala, S.S., Lustig, M., 2020. Extreme MRI: Large-scale volumetric dynamic imaging from continuous non-gated acquisitions. *Magn. Reson. Med.* 84, 1763–1780. doi:[10.1002/mrm.28235](https://doi.org/10.1002/mrm.28235).
- ⁴³² Pipe, J.G., Farthing, V.G., Forbes, K.P., 2002. Multishot diffusion-weighted FSE using PROPELLER MRI. *Magn. Reson. Med.* 47, 42–52. doi:[10.1002/mrm.10014](https://doi.org/10.1002/mrm.10014).
- ⁴³⁵ Porter, D.A., Heidemann, R.M., 2009. High resolution diffusion-weighted imaging using readout-segmented echo-planar imaging, parallel imaging and a two-dimensional navigator-based reacquisition. *Magn. Reson. Med.* 62, 468–475. doi:[10.1002/mrm.22024](https://doi.org/10.1002/mrm.22024).

- 439 Pruessmann, K.P., Weiger, M., Scheidegger, M.B., Boesiger, P., 1999.
440 SENSE: Sensitivity encoding for fast MRI. Magn. Reson. Med. 42, 952–
441 962. doi:[10.1002/\(SICI\)1522-2594\(199911\)42:5<952::AID-MRM16>3.0.CO;2-S](https://doi.org/10.1002/(SICI)1522-2594(199911)42:5<952::AID-MRM16>3.0.CO;2-S).
- 443 Ra, J.B., Rim, C.Y., 1993. Fast imaging using subencoding data sets from
444 multiple detectors. Magn. Reson. Med. 30, 142–145. doi:[10.1002/mrm.1910300123](https://doi.org/10.1002/mrm.1910300123).
- 446 Roemer, P.B., Edelstein, W.A., Hayes, C.E., Souza, S.P., Mueller, O.M.,
447 1990. The NMR phased array. Magn. Reson. Med. 16, 192–225. doi:[10.1002/mrm.1910160203](https://doi.org/10.1002/mrm.1910160203).
- 449 Shafieizargar, B., Jeurissen, B., Poot, D.H.J., Klein, S., Van Audekerke,
450 J., Verhoye, M., den Dekker, A.J., Sijbers, J., 2023. ADEPT: Accurate
451 diffusion echo-planar imaging with multi-contrast shTs. Magn. Reson.
452 Med. 89, 396–410. doi:[10.1002/mrm.29398](https://doi.org/10.1002/mrm.29398).
- 453 Tournier, J.D., Calamante, F., Connelly, A., 2007. Robust determination
454 of the fibre orientation distribution in diffusion MRI: Non-negativity con-
455 strained super-resolved spherical deconvolution. NeuroImage 35, 1459–
456 1472. doi:[10.1016/j.neuroimage.2007.02.016](https://doi.org/10.1016/j.neuroimage.2007.02.016).
- 457 Truong, T.K., Guidon, A., 2014. High-resolution multishot spiral diffusion
458 tensor imaging with inherent correction of motion-induced phase errors.
459 Magn. Reson. Med. 71, 790–796. doi:[10.1002/mrm.24709](https://doi.org/10.1002/mrm.24709).
- 460 Trzasko, J., Manduca, A., 2011. Local versus global low-rank promotion in

- ⁴⁶¹ dynamic MRI series reconstruction, in: Proceedings of the 19th Annual
⁴⁶² Meeting of ISMRM, Montréal, CAN, p. 4371.
- ⁴⁶³ Tuch, D.S., Reese, T.G., Wiegell, M.R., Makris, N., Belliveau, J.W., Wedeen,
⁴⁶⁴ V.J., 2002. High angular resolution diffusion imaging reveals intravoxel
⁴⁶⁵ white matter fiber heterogeneity. Magn. Reson. Med. 48, 577–582. doi:[10.1002/mrm.10268](#).
- ⁴⁶⁶
- ⁴⁶⁷ Uecker, M., Lai, P., Murphy, M.J., Virtue, P., Elad, M., Pauly, J.M.,
⁴⁶⁸ Vasanawala, S.S., Lustig, M., 2014. ESPIRiT – an eigenvalue approach
⁴⁶⁹ to autocalibrating parallel MRI: Where SENSE meets GRAPPA. Magn.
⁴⁷⁰ Reson. Med. 71, 990–1001. doi:[10.1002/mrm.24751](#).
- ⁴⁷¹ Veraart, J., Novikov, D.S., Christiaens, D., Ades-aron, B., Sijbers, J., Fiere-
⁴⁷² mans, E., 2016. Denoising of diffusion mri using random matrix theory.
⁴⁷³ NeuroImage 142, 394–406. doi:[10.1016/j.neuroimage.2016.08.016](#).
- ⁴⁷⁴ Wu, W., Koopmans, P.J., Andersson, J.L., Miller, K.L., 2019. Diffusion
⁴⁷⁵ Acceleration with Gaussian process Estimated Reconstruction (DAGER).
⁴⁷⁶ Magn. Reson. Med. 82, 107–125. doi:[10.1002/mrm.27699](#).
- ⁴⁷⁷ Zhang, T., Pauly, J.M., Levesque, I.R., 2015. Accelerated parameter mapping
⁴⁷⁸ with a locally low rank constraint. Magn. Reson. Med. 73, 655–661. doi:[10.1002/mrm.25161](#).
- ⁴⁷⁹